

# Bandwidth and conversion efficiency analysis of dissipative Kerr soliton frequency combs based on bifurcation theory

Janina Gärtner, Philipp Trocha, Rainer Mandel,  
Christian Koos, Tobias Jahnke, Wolfgang Reichel

CRC Preprint 2018/56, December 2018

KARLSRUHE INSTITUTE OF TECHNOLOGY

CRC 1173



Wave  
phenomena

## Participating universities



**Universität Stuttgart**

EBERHARD KARLS  
UNIVERSITÄT  
TÜBINGEN



**Funded by**

**DFG**

ISSN 2365-662X

# Bandwidth and Conversion Efficiency Analysis of Dissipative Kerr Soliton Frequency Combs Based on Bifurcation Theory

J. Gärtner,<sup>1</sup> P. Trocha,<sup>2</sup> R. Mandel,<sup>1</sup> C. Koos,<sup>2</sup> T. Jahnke,<sup>3</sup> and W. Reichel<sup>1,\*</sup>

<sup>1</sup>*Institute for Analysis (IANA), Karlsruhe Institute of Technology, 76131 Karlsruhe, Germany*

<sup>2</sup>*Institute of Photonics and Quantum Electronics (IPQ),  
Karlsruhe Institute of Technology, 76131 Karlsruhe, Germany*

<sup>3</sup>*Institute for Applied and Numerical Mathematics (IANM),  
Karlsruhe Institute of Technology, 76131 Karlsruhe, Germany*

Dissipative Kerr soliton frequency combs generated in high-Q microresonators may unlock novel perspectives in a variety of applications and crucially rely on quantitative models for systematic device design. Here, we present a global bifurcation study of the Lugiato-Lefever equation which describes Kerr comb formation. Our study allows systematic investigation of stationary comb states over a wide range of technically relevant parameters. Quantifying key performance parameters of bright and dark-soliton combs, our findings may serve as a design guideline for Kerr comb generators.

## I. INTRODUCTION AND MAIN RESULTS

Kerr frequency combs have the potential to revolutionize a variety of applications such as high-speed data transmission [1–3], high-precision optical ranging [4, 5] and spectroscopy [6] as well as highly accurate optical frequency synthesis [7]. Kerr frequency combs stand out due to their high optical bandwidth that may exceed an octave of frequencies, narrow linewidths down to 1 kHz, and large line spacings of tens of GHz [8–10]. Moreover, Kerr comb generators feature small footprint and are amenable to efficient wafer-level mass production, thereby paving the path to large-scale industrial deployment. On a physical level, Kerr comb generators rely on third-order nonlinear interaction in high-Q microresonators that are pumped by a continuous-wave (CW) laser [11]. Under appropriate pump conditions, cascaded degenerate and nondegenerate four-wave mixing (FWM) can lead to a soliton waveform that circulates in the cavity, balancing self-phase modulation and dispersion as well as cavity loss and parametric gain [12]. These dissipative Kerr soliton (DKS) combs consist of strictly equidistant phase-locked optical tones and stand out due to smooth spectral envelopes and extraordinary robustness with respect to variations of the pump conditions. Mathematically, Kerr frequency comb generators are represented by nonlinear systems with rather complex dynamics. Systematic design and theory-guided improvement of Kerr comb sources therefore require reliable mathematical models that cover practically relevant parameter spaces and that combine intuitive qualitative understanding with quantitatively correct predictions of the behavior of the nonlinear system. Kerr comb dynamics are described by the Lugiato-Lefever equation (LLE), a damped, driven and detuned nonlinear Schrödinger equation [13–15]. The LLE has been extensively studied, using, e.g., numerical simulations of the temporal comb formation dynamics, which have reached remarkable accu-

racy in predicting and explaining experimental results [16, 17]. However, time-domain integration of the LLE allows only to access specific comb states that strongly depend on the individual device parameters as well as on the complex interplay of the initial conditions and the time-dependent tuning of the pump. Specifically, time-integration techniques do not permit to globally study the variety of different stationary Kerr comb states that can be accessed by exploiting the full range of technically accessible device and operation parameters. This gap can be closed by bifurcation analysis, which allows to investigate the structure of stationary solutions and to obtain qualitative as well as quantitative insights. So far, stationary states of the LLE have been mainly investigated by local bifurcation analysis [14, 15, 18–23], focusing on states in the vicinity of the trivial LLE solution that consists of a single CW tone at the pumped resonance. Global aspects in particular concerning the snaking behavior of solution branches are discussed in [15, 19, 20], and recently a rigorous stability analysis of stationary states closing the gap between linearized stability and nonlinear stability was achieved in [24]. These methods revealed a large variety of comb states, and were partially extended via numerical continuation methods to regions further away from the trivial state where solitons occur. However, a global study that identifies pronounced soliton states and favorable operation regimes across the full range of technical accessible device and operation parameters has not been presented so far.

In this paper, we present a global bifurcation study of the LLE, covering a large space of technically accessible parameters. Our analysis comprises both bright-soliton states in resonators with anomalous group-velocity dispersion (GVD) [12] as well as dark solitons that form in the presence of normal GVD [25]. For both types of combs, we classify branches associated with single and multi-soliton states and characterize single-soliton states by their optical bandwidth as well as by the pump-to-comb power transfer efficiency. Our bifurcation analysis hence allows determining and systematically optimizing the performance of Kerr comb generators in integrated

---

\* wolfgang.reichel@kit.edu

photonic systems, which is of significant importance for industrial adoption of these devices.

This paper is organized as follows: In Section II, we introduce the Lugiato-Lefever equation and derive sufficient conditions for bifurcations from the trivial state. In Section III, we identify bifurcation branches leading to single-soliton states and investigate the behavior of the soliton and its characteristics along these branches. Section IV is dedicated to a quantitative characterization of single-soliton frequency combs using the bandwidth and the power conversion efficiency as performance metrics. Mathematical details and derivations can be found in the Appendix.

## II. BIFURCATION ANALYSIS FOR THE LUGIATO-LEFEVER EQUATION

We start our analysis from the Lugiato-Lefever equation

$$i \frac{\partial a}{\partial t} = -da'' - (i - \zeta)a - |a|^2 a + if = 0 \quad (1)$$

and its stationary version

$$-da'' - (i - \zeta)a - |a|^2 a + if = 0. \quad (2)$$

Here,  $a(t, x)$  is a  $2\pi$ -periodic function that represents the optical intracavity field,  $d$  is the group velocity dispersion parameter, and  $\zeta$  the detuning of the input pump laser as a free real-valued parameter. The forcing  $f$  corresponds to the amplitude of the optical driving field. Relations that connect the normalized quantities  $d, \zeta, f$  to their physical counterparts can be found in Appendix D. In the following we consider  $2\pi$ -periodic solutions  $a$  of Eq. (2) which feature even symmetry about  $x = \pi$  and therefore fulfill the Neumann boundary conditions

$$a'(0) = a'(\pi) = 0. \quad (3)$$

Thus, from now on we restrict our attention to functions  $a : [0, \pi] \rightarrow \mathbb{C}$  which satisfy Eq. (2) on  $[0, \pi]$  together with Eq. (3). In Fourier modes the solution is represented as  $a(x) = \sum_{k \in \mathbb{Z}} \hat{a}_k e^{ikx}$  with  $\hat{a}_{-k} = \hat{a}_k$ . The intracavity power of the field is given by the square of the  $L^2$ -norm  $\|a\|_2^2 := \sum_{k \in \mathbb{Z}} |\hat{a}_k|^2$ . There are trivial solutions  $a_0$  of Eqs. (2), (3) which are complex constants. Let us assume that the trivial solution  $a_0$  can be parametrized (locally) as  $a_0 = a_0(\zeta)$ .<sup>1</sup> As an example, the curve  $(\zeta, a_0(\zeta))$  of constant solutions is shown in black for  $f = 2$  in Fig. 1a) in case of anomalous dispersion ( $d = 0.1$ ) and in Fig. 1d) in case of normal dispersion ( $d = -0.1$ ). For

each  $\zeta$  the squared  $L^2$ -norm of  $a_0(\zeta)$  is plotted. Note that three different constant solutions exist for certain values of  $\zeta$ . Nontrivial solutions, associated with frequency combs, may arise from the curve of trivial solutions at bifurcation points, which can be defined in the simplest form applicable for our purposes as follows: A point  $P = (\zeta_0, a_0(\zeta_0)) \in \mathbb{R} \times \mathbb{C}$  on the trivial curve is called a bifurcation point for Eqs. (2), (3) if there exists a second curve  $(\zeta_s, a_s)$  of solutions of Eqs. (2), (3), which is parameterized by  $s$  in some interval and crosses transversally the trivial curve at  $P$ .

The structure of the solution set near  $(\zeta_0, a_0(\zeta_0))$  depends on the properties of the linearized operator  $L$

$$L\phi := -d\phi'' - (i - \zeta_0)\phi - 2|a_0|^2\phi - a_0^2\bar{\phi}, \quad (4a)$$

$$\phi'(0) = \phi'(\pi) = 0. \quad (4b)$$

Because of the implicit function theorem, cf. [26, Theorem I.1.1], nontrivial solutions can only bifurcate from the trivial branch at  $(\zeta_0, a_0(\zeta_0))$  if the kernel  $\text{Ker } L = \{\phi : L\phi = 0, \phi'(0) = \phi'(\pi) = 0\}$  is at least one-dimensional. This is the case provided that there is an integer  $k \in \mathbb{N}$  such that

$$(\zeta_0 + dk^2)^2 - 4|a_0(\zeta_0)|^2(\zeta_0 + dk^2) + 1 + 3|a_0(\zeta_0)|^4 = 0. \quad (5)$$

Solving Eq. (5) yields

$$k_{1,2} := \sqrt{\frac{2|a_0(\zeta_0)|^2 - \zeta_0 \pm \sqrt{|a_0(\zeta_0)|^4 - 1}}{d}}. \quad (6)$$

For details on the derivation of Eqs. (5) and (6) see Appendix A. The wave number  $k_{1,2}$  obtained by evaluating the expression on the right side of Eq. (6) defines the spatial periodicity  $2\pi/k_{1,2}$ , after which the nontrivial comb state in the vicinity of the bifurcation point repeats itself, i.e.,  $a(x) = a(x + 2\pi/k_{1,2})$ . Equations (5) and (6) naturally occur in bifurcation studies of Eq. (2). In [14, 15, 19], for instance, bifurcations are considered from the point of view of spatial dynamics both for normal and anomalous dispersion, and parameter regimes are determined where Turing patterns as well as 1-soliton states bifurcate from trivial solutions. In [20] a similar approach is taken to study bifurcation of dark solitons from trivial solutions in the normal-dispersion regime. In most of these works, bifurcations with respect to the forcing parameter  $f$  are studied and the  $2\pi$ -periodicity of the solutions is neglected. In contrast, our work takes into account the  $2\pi$ -periodicity and our goal is a global picture of all branches bifurcating from the trivial solution with respect to the detuning  $\zeta$ , whose physical accessible parameter space is usually larger than the parameter space for  $f$ . With the help of Eq. (6) we can formulate the following bifurcation result, that explains under which conditions bifurcations from the line of trivial solutions occur.

*For a point  $P = (\zeta_0, a_0(\zeta_0))$  on the curve of trivial solutions the following is true:*

<sup>1</sup> This assumption is for simplicity of the presentation. It fails only at the turning points of the trivial curve, which does not lead to any undesirable effect. Other parametrizations  $\zeta_0 = \zeta_0(t), a_0 = a_0(t)$  are also possible, cf. [21].

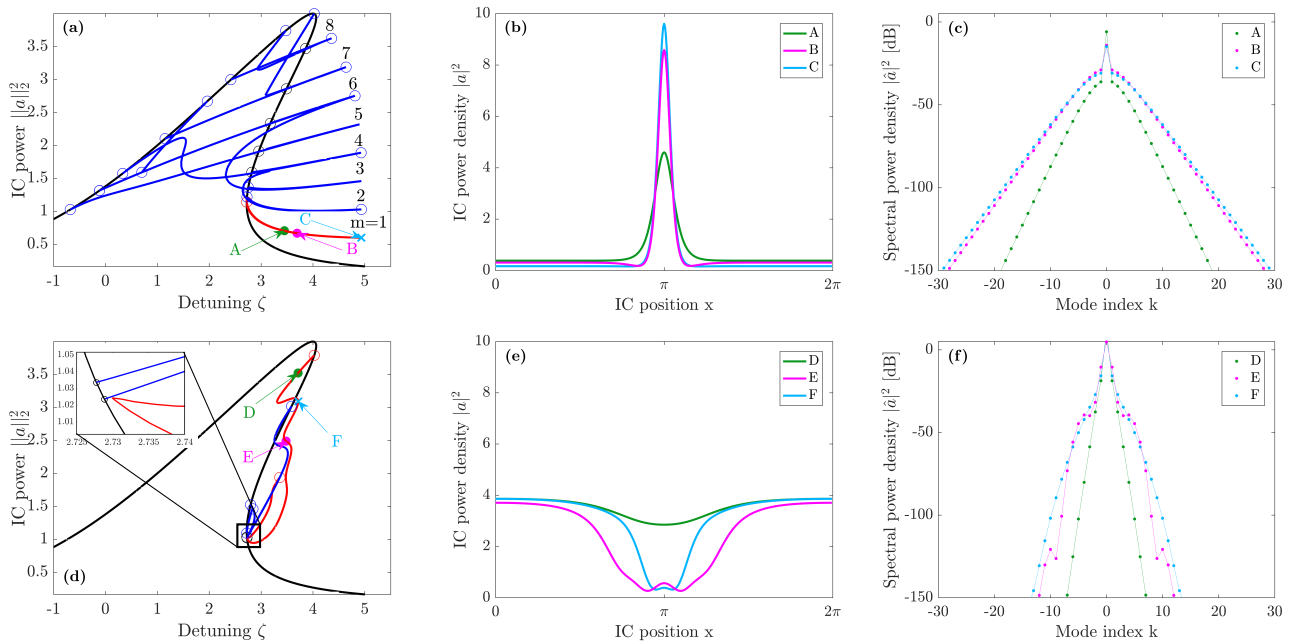


FIG. 1: Bifurcation maps and nontrivial comb states for bright solitons in anomalous-dispersion ( $d > 0$ , top) and dark solitons in normal-dispersion microresonators ( $d < 0$ , bottom). a) Bifurcation map of the LLE for  $f = 2$  and  $d = 0.1$  indicating the normalized intracavity power  $\|a\|_2^2$  vs. the normalized detuning  $\zeta$ . The constant solution is indicated in black, the single soliton state bifurcation branch ( $m = 1$ ) in red, while blue corresponds to other bifurcation branches of multi-soliton states with  $m = 2, \dots, 8$  pulses circulating in the cavity. Circles indicate bifurcation points. b) Spatial power distribution as a function of normalized intracavity position  $x$  of single-soliton states corresponding to points A, B and to the turning point C indicated in Subfigure a). c) Spectral power distribution of single-soliton states corresponding to points A, B and to the turning point C indicated in Subfigure a). Note that for illustrative purposes a relatively low forcing  $f = 2$  was chosen, resulting in a quick drop of the power of spectral modes further away from the pump. Here the bifurcation-and-continuation method is sufficiently precise to correctly predict spectral components which are more than 150 dB below the pump, hence safely covering technical relevant power ranges. d) Bifurcation map of the LLE for  $f = 2$  and  $d = -0.1$  indicating the normalized intracavity power  $\|a\|_2^2$  vs. the normalized detuning  $\zeta$ . Black denotes again the constant solution, red the single-soliton state bifurcation branch, and blue corresponds to other bifurcation branches. Here, circles also mark bifurcation points. e) Spatial power distribution as a function of normalized intracavity position  $x$  of single-soliton states corresponding to points D, E and to the turning point F indicated in Subfigure d). f) Spectral power distribution of single-soliton states corresponding to points D, E and to the turning point F indicated in Subfigure d).

- (i) If exactly one of the two numbers  $k_{1,2}$  from Eq. (6) is an integer and if the transversality condition

$$2|a_0(\zeta_0)|^4(|a_0(\zeta_0)|^2 - \zeta_0) \mp (1 + \zeta_0^2 - |a_0(\zeta_0)|^4)\sqrt{|a_0(\zeta_0)|^4 - 1} \neq 0 \quad (7)$$

holds with “-” if  $k_1 \in \mathbb{N}$  and “+” if  $k_2 \in \mathbb{N}$ , then  $P$  is a bifurcation point for Eqs. (2), (3).

- (ii) If neither  $k_1$  nor  $k_2$  is an integer, then  $P$  is not a bifurcation point for Eqs. (2), (3), and near  $P$  only trivial solutions of Eqs. (2), (3) exist.

In the remaining cases, where either the condition (7) fails or both  $k_1$  and  $k_2$  are integers, no statement is made. The result mainly goes back to Theorem 4 in [21]. Compared to [21] its present formulation as well as its proof allow substantial simplifications, see Appendix B.

For the cases  $f = 2$ ,  $d = \pm 0.1$  we have numerically computed the bifurcation points determined by Eq. (5). We also checked for all bifurcation points which one of the numbers  $k_{1,2}$  in Eq. (6) is an integer, and whether the transversality condition (7) holds, cf. Table I. The computed bifurcation points on the trivial branch are marked by circles in Fig. 1a) and d) for  $d = 0.1$  and  $d = -0.1$  respectively. In case (i) of the above result we may apply Rabinowitz’ global bifurcation theorem from [27] in combination with Theorem 4 in [21]. As a result we obtain that a branch bifurcating from the trivial curve at  $(\zeta_0, a_0(\zeta_0))$  either returns to the trivial curve at some other bifurcation point or joins another branch of nontrivial solutions.

In Fig. 1a) a complete picture of all branches bifurcating from the trivial branch is shown for anomalous dis-

persion with  $d = 0.1$ . For clarity of the figures, we did not include any secondary bifurcation branches, i.e., branches not directly coming off the trivial branch. The analytical and numerical description of secondary bifurcations coming with the effect of period-doubling, -tripling etc. is provided in [28]. The branches were computed by the software `pde2path` (cf. [29, 30]) which is designed to numerically treat continuation and bifurcation of PDE systems. Given a starting point on the trivial branch together with a tangent direction, `pde2path` starts a continuation algorithm to compute the trivial branch. Whenever a simple eigenvalue of the linearization crosses zero, a bifurcation point is detected and the bifurcating branch can be followed.

For the example given in Fig. 1a), all calculated bifurcation points in Table I were reproduced by `pde2path`. Bifurcation branches determined by `pde2path` are shown in Fig. 1a) as colored lines. Here, the single-soliton branch ( $m = 1$ ) is highlighted in red. Blue branches are related to higher-order soliton frequency combs ( $m = 2, \dots, 8$ ). Note that the bifurcation branches seem to stop at the points where a maximal value of  $\zeta$  is reached. But in fact, these points are turning points, and each branch continues in opposite direction on nearly the same path. In Fig. 1d) the same analysis is performed for normal dispersion ( $d = -0.1$ ). The single-dark-soliton branch is again marked in red. Note that `pde2path` does not only generate the bifurcation map, but also allows to calculate the stationary solutions of the LLE along the various branches.

### III. SOLITONS ALONG BIFURCATING BRANCHES

For a global study, we use `pde2path` to explore a much more extensive parameter space aiming at the detection of 1-soliton states on bifurcating branches. Based on a large number of numerical experiments, we developed heuristics that allow to identify branches with single-soliton states and to find the solitons with the strongest spatial localization. Let us number the bifurcation points and bifurcating branches along  $a_0(\zeta)$  starting from the left end of the trivial branch.

- (i) For anomalous dispersion ( $d > 0$ ) bright 1-solitons occur on the last bifurcating branch. The most localized 1-solitons occur near the first turning point of this branch (locally maximizing  $\zeta$ ), cf. Fig. 1a).
- (ii) For normal dispersion ( $d < 0$ ) dark 1-solitons occur on the first bifurcating branch. The most localized 1-solitons occur near the second turning point of this branch (locally maximizing  $\zeta$ ), cf. Fig. 1d).

These heuristics are illustrated in Fig. 2, where the full-width at half-maximum ( $\text{FWHM}_a$ ) in case of bright solitons as well as the full-width at half-minimum ( $\text{FWHM}_i$ ) in case of dark solitons is plotted for the spatial field

$\zeta_0$	$a_0(\zeta_0)$	$k_1$	$k_2$	Transv.
-0.6770	$0.51 + 0.87i$	5.44	5	3.67
-0.1117	$0.66 + 0.94i$	6	4.35	5.56
0.3325	$0.79 + 0.98i$	6.35	4	4.49
1.1508	$1.05 + 1.00i$	7	3.47	12.26
1.9646	$1.34 + 0.94i$	7.65	3	4.44
2.4179	$1.50 + 0.87i$	8	2.74	16.42
3.4759	$1.87 + 0.49i$	8.72	2	4.12
4.0242	$2.00 - 0.05i$	8.85	1	3.85
3.8603	$1.73 - 0.68i$	8	1.56i	-22.26
3.4893	$1.43 + 0.90i$	7	2.13i	-23.74
3.1793	$1.17 - 0.99i$	6	2.49i	-21.14
2.9576	$0.96 - 1.00i$	5	2.76i	-17.57
2.8218	$0.80 - 0.98i$	4	2.96i	-14.19
2.7541	$0.68 - 0.95i$	3	3.09i	-11.41
2.7293	$0.61 - 0.92i$	2	3.14i	-9.32
2.7239	$0.57 - 0.90i$	1	3.15i	-8.00

TABLE I: Bifurcation points on the trivial branch for anomalous dispersion  $d = 0.1$ ,  $f = 2$ . The coordinates  $(\zeta_0, a_0(\zeta_0))$  shown in the first two columns are determined so that at least one of the values  $k_{1,2}$  (third and fourth column) from Eq. (6) is an integer. The integer value of either  $k_1$  or  $k_2$  determines the periodicity of the field in the vicinity of the corresponding bifurcation point. The last column lists the values obtained from evaluating the left side of Eq. (7) in order to determine whether the transversality condition is fulfilled.

distribution along the bifurcating branch starting from the initial bifurcation point. Note that the bright 1-soliton at point C in Fig. 1 a) has slightly smaller  $\text{FWHM}_a = 0.3330$  than the bright 1-soliton at label B ( $\text{FWHM}_a = 0.3393$ ). Both for normal and anomalous dispersion, the common feature of the most localized 1-solitons is their occurrence at maximum possible detuning values within all turning points of the bifurcating branch. These heuristics are illustrated in Fig. 1. For different points A, B, C along the bright-single-soliton branch and D, E, F along the dark-single-soliton branch respectively, comb states are depicted in the spatial and frequency domain in Fig. 1 b), c) and e), f). As expected, the comb states with the smallest  $\text{FWHM}_{a/i}$  identified in points C and F by using the aforementioned heuristics show the strongest localization in the spatial domain. Furthermore, we can see that in the case of anomalous dispersion, there is no other state on the branch  $m = 1$  for the same value of  $\zeta$ . However, in the case of normal dispersion, we find another dark-soliton state with equal detuning marked by point D in Fig. 1d), as e.g. discussed in [14]. Yet point F in Fig. 1 d) shows a stronger spatial localization, cf. Fig. 2, and has a broader frequency comb than D.

In this example the soliton character of the solutions,

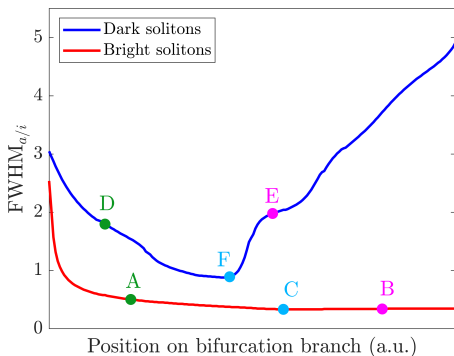


FIG. 2: Full-width at half-maximum ( $\text{FWHM}_a$ ) of bright solitons along the bifurcating branch for anomalous dispersion (red,  $d = 0.1$ ) and full-width at half-minimum ( $\text{FWHM}_i$ ) of dark solitons for normal dispersion (blue,  $d = -0.1$ ) for  $f = 2$ .

i.e., their strong localization in the spatial domain at the turning point is visible but not yet very pronounced due to the moderate value of  $f$ . With increasing  $f$  the soliton localization as well as the comb power and comb bandwidth will be much enhanced. At the same time the graphs of the bifurcation branches will be less illustrative due to a steeply increasing number and density of bifurcation points. Therefore,  $f = 2$  is chosen merely for illustrative reasons, and much larger ranges of  $f$  are covered in Section IV.

#### IV. QUANTITATIVE CHARACTERIZATION OF SOLITON FREQUENCY COMBS

Using the heuristics from the previous section, we are able to identify single-soliton states with the strongest spatial localization for a certain forcing both in the normal as well as anomalous-dispersion regime. Based on this approach, we now characterize these comb states  $a(x) = \sum_{k \in \mathbb{Z}} \hat{a}_k e^{ikx}$  by their comb bandwidth  $2k^*$  and their power conversion efficiency (PCE)  $\eta$ . The comb bandwidth is quantified by the 3dB-point, i.e., by the minimal integer  $k^*$  that fulfills  $|\hat{a}_{k^*}|^2 \leq \frac{1}{2} |\hat{a}_1|^2$ . Note that the 3-dB comb bandwidth is defined with respect to the power  $|\hat{a}_1|^2$  of the mode directly adjacent to the pumped mode rather than the power  $|\hat{a}_0|^2$  of the pumped mode itself, which is usually much stronger than all other modes of the comb. The PCE is the ratio between the intracavity comb power

$$P_{\text{FC}} = \sum_{k \in \mathbb{Z} \setminus \{0\}} |\hat{a}_k|^2 \quad (8)$$

and the pump power  $f^2$ . Note that the intracavity comb power does not contain the zero mode, since  $|\hat{a}_0|^2$  mostly stems from the pump and is therefore non-zero even if no comb is formed in the microresonator. For bright solitons

(BS), under the assumption of small damping and small forcing, approximation formulas for the comb bandwidth as well as the PCE exist, cf. [12, 31–34]. Assuming a detuning set to the maximum value that permits a single soliton  $\zeta_{\text{BS,max}} = \pi^2 f^2 / 8$  [12, 32], they read as follows,

$$2k_{\text{BS,max}}^* \approx \sqrt{2} \ln(1 + \sqrt{2}) \frac{f}{\sqrt{d}}, \quad (9a)$$

$$\eta_{\text{BS,max}} \approx \frac{1}{f} \sqrt{\frac{d}{2}}. \quad (9b)$$

More details on these equations can be found in Appendix C. Expressions for the approximation of dark solitons resembling a flipped sech function on top of a cw-background are given in [20], compare the green curve in Fig. 1e). They are valid near the bifurcation point and are obtained using multiple scale asymptotic. As mentioned before, this kind of solitons, indicated in Fig. 1d) by point D, is of less interest due to its weaker localization, reduced comb bandwidth and power compared to the dark soliton at point F. For dark solitons of the latter type no formula for the comb bandwidth or PCE is available to the best of our knowledge.

For dispersion parameters  $d = \pm 0.1, \pm 0.15, \pm 0.2, \pm 0.25$  and  $f > 1$ , we have carried out a large parameter study. For  $d > 0$  we computed the last bifurcation point and its corresponding bifurcating branch. Based on the heuristics in Section III we stopped the computation as soon as we reached the first turning point, i.e. point C in Fig. 1a), where the most localized bright soliton is found. In the same manner the strongest localized dark solitons in the case  $d < 0$  are at the second turning point of the first bifurcating branch, i.e. point F in Fig. 1d). For all of the above values of the dispersion  $d$  and the pump power  $f$ , the corresponding solitons at the turning point were investigated and their comb bandwidth as well as their PCE were evaluated.

The results are plotted in Fig. 3. For bright solitons, gray lines corresponding to the approximate expressions in Eq. (9a) and Eq. (9b) are also shown in a) and c). As mentioned before, the validity of these approximations is guaranteed only for small damping, small forcing and large forcing/damping ratio [33, 34]. This explains the deviations from the curves computed by numerical bifurcation and continuation which occur for PCE in the small  $f$  regime (damping in (2) is set to 1) in Fig. 3c) and for comb bandwidth in the large  $f$  regime in Fig. 3a). The comb bandwidth increases with an increasing  $f$  at the expense of a decreasing conversion efficiency. Additionally, one can see that with  $d \rightarrow 0$  the comb bandwidth increases whereas the PCE decreases.

For dark solitons, the overall dependence of the conversion efficiency and comb bandwidth shows the same trends as for bright solitons, see Fig. 3b) and d). In direct comparison, dark solitons have a decreased bandwidth along with a higher conversion efficiency for the same values of  $f$  and  $|d|$ . We attribute this to the strong constant background of the dark solitons in the spatial do-

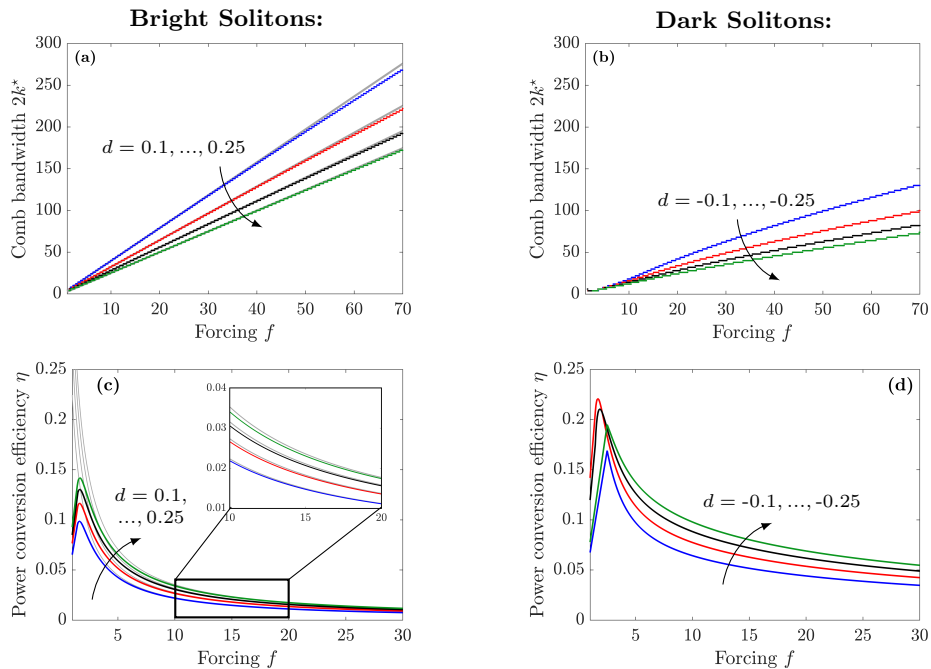


FIG. 3: Bandwidths  $2k^*$  and power conversion efficiencies (PCE)  $\eta$  for bright-soliton (a,c) and dark-soliton (b,d) combs as a function of the forcing  $f$  and dispersion  $d = \pm 0.1, \pm 0.15, \pm 0.2, \pm 0.25$ . a) Bandwidth of bright-soliton combs obtained by numerical bifurcation and continuation (NBC, colored solid lines) along with an approximation according to Eq. (9a). The linear approximation is in good agreement with the numerical results and deviates only for a strong forcing. A stronger dispersion leads to a decreasing comb bandwidth. b) Bandwidth of dark-soliton combs obtained by NBC. c) PCE of bright-soliton states obtained by NBC (colored solid lines) along with an approximation according to Eq. (9b) (gray dashed lines). The approximation is in good agreement with the numerical results, but deviates strongly for weak forcing. A weaker dispersion leads to a decreasing PCE. d) PCE of dark-soliton states obtained by NBC. The PCE decreases with an increasing forcing, but is overall higher as for bright solitons. Here, weaker dispersion also leads to a decreasing PCE.

main which enables a more efficient power transfer from the continuous-wave pump to the soliton. However, the increased spatial width of the dark solitons is also linked to a narrower frequency comb in the spectral domain. We note that the comb bandwidth of both bright and dark solitons does not increase strictly linearly with an increasing forcing. For dark solitons the nonlinear behavior is more pronounced.

For the physical properties of soliton frequency combs in non-normalized units, the bandwidth  $2k^*$  as well as the conversion efficiency  $\eta$  have to be converted. The physical comb bandwidth  $\Delta\omega/(2\pi)$  is obtained by multiplying  $2k^*$  with the free spectral range FSR of the resonator, i.e., the inverse of the round-trip time  $T_R$  of the light inside

$$\Delta\omega/(2\pi) = \text{FSR} \times 2k^* = T_R^{-1} \times 2k^*. \quad (10)$$

To determine the physical conversion efficiency outside the resonator  $\eta_{\text{out}}$ , the physical power coupling coefficient  $\kappa$  between the bus waveguide and the microresonator as well as the physical round-trip-power-loss coefficient  $\alpha$  have to be taken in consideration

$$\eta_{\text{out}} = \frac{4\kappa^2}{(\alpha + \kappa)^2} \eta. \quad (11)$$

For details on (11), see Appendix D. In order to achieve high external power conversion efficiencies  $> 30\%$  as, e.g., in [35], an *overcoupled* resonator with  $\alpha \ll \kappa$  is preferable. As visible in Fig. 3c) and d), a microresonator with normal dispersion enabling dark soliton states will tend to improve the PCE. It should be noted, however that the generation of normal-dispersion frequency combs generally requires an avoided mode crossing for initial modulation instability [25], which makes the design of the device more complex.

## V. SUMMARY

We have performed a global bifurcation analysis of the Lugiato-Lefever equation and provided an overview on the structure of nontrivial solutions. We find single-soliton frequency combs both in the normal and anomalous-dispersion regime. Our investigation covers a broad space of technically relevant device and operation parameters. It allows us to identify the broadest soliton combs and to benchmark them with respect to bandwidth and pump-to-comb power conversion effi-

ciency. Our findings are in good agreement with simplified analytic models. Comparing the results for bright and dark solitons, we find that dark solitons outperform bright solitons significantly in terms of power conversion efficiency at the expense of a reduced bandwidth.

The bifurcation and continuation method allows to determine the performance parameters of single-soliton comb states even for the cases where simplified analytic models are not valid, e.g., for certain dark solitons. Our approach can be further extended to include additional effects such as two-photon absorption and to study their impact on the stationary comb states, see [36]. The results of our

investigation allow for targeted design of soliton comb generators for specific applications. In this context, the power conversion efficiency and the comb bandwidth are key performance characteristics that need to be optimized under technical restrictions such as limited optical input power.

## ACKNOWLEDGMENTS

The authors gratefully acknowledge financial support by the Deutsche Forschungsgemeinschaft (DFG) through CRC 1173.

## APPENDIX A: IDENTIFICATION OF BIFURCATION POINTS

Here we derive the expression that allows to identify bifurcation points on the curve of trivial solutions to the stationary Lugiato-Lefever equation with Neumann boundary conditions

$$-da'' - (i - \zeta)a - |a|^2a + if = 0, \quad (\text{A1})$$

$$a'(0) = a'(\pi) = 0. \quad (\text{A2})$$

The structure of solutions  $a : [0, \pi] \rightarrow \mathbb{C}$  depends on the properties of the linearized operator  $L$

$$L\phi := -d\phi'' - (i - \zeta_0)\phi - 2|a|^2\phi - a^2\bar{\phi}, \quad (\text{A3a})$$

$$\phi'(0) = \phi'(\pi) = 0. \quad (\text{A3b})$$

We denote the kernel of the differential operator  $L$  by  $\text{Ker } L = \{\phi : L\phi = 0, \phi'(0) = \phi'(\pi) = 0\}$  and its range by  $\text{Rg } L = \{L\phi : \phi'(0) = \phi'(\pi) = 0\}$ , where the functions  $\phi : [0, \pi] \rightarrow \mathbb{C}$  are twice continuously differentiable. For such a function  $\phi \neq 0$  we denote by  $\text{span}\{\phi\} = \{t\phi : t \in \mathbb{R}\}$  the one-dimensional space of all real multiples of  $\phi$  and by  $\text{span}\{\phi\}^\perp = \{\psi : \int_0^\pi \phi(x)\bar{\psi}(x) dx = 0\}$  its  $L^2$ -orthogonal complement. In the following we write  $a_0$  instead of  $a_0(\zeta_0)$ , but we keep the notation  $a_0(\zeta)$  if we want to stress the  $\zeta$ -dependence of the trivial solution. Let us abbreviate the nonlinearity in Eq. (A1) by  $g(a) = |a|^2a - if$ . The derivative  $Dg(a)z := \frac{d}{dt}g(a + tz)|_{t=0} = 2|a|^2z + a^2\bar{z}$  for  $a, z \in \mathbb{C}$  can also be written in the form

$$Dg(a)z = \begin{pmatrix} 3(\text{Re } a)^2 + (\text{Im } a)^2 & 2 \text{Re } a \text{Im } a \\ 2 \text{Re } a \text{Im } a & (\text{Re } a)^2 + 3(\text{Im } a)^2 \end{pmatrix} \begin{pmatrix} \text{Re } z \\ \text{Im } z \end{pmatrix}. \quad (\text{A4})$$

Note that  $Dg(a)$  appears in the definition (A3) of the linearized operator  $L$ . Besides the linearized operator  $L$  given in Eq. (A3) we also consider its adjoint operator

$$L^*\phi = -d\frac{d^2}{dx^2}\phi + (i + \zeta_0)\phi - \overline{Dg(a_0(\zeta_0))}\phi, \quad \phi'(0) = \phi'(\pi) = 0, \quad (\text{A5})$$

which will be used below. Next we will compute the spaces  $\text{Ker } L$ ,  $\text{Ker } L^*$ , which have the same finite dimension since both  $L$  and  $L^*$  are Fredholm operators. Owing to the Neumann boundary conditions, any element  $\phi \in \text{Ker } L$  can be expanded in the form  $\phi(x) = \sum_{l=0}^\infty \alpha_l \cos(lx)$ . Since  $\{\cos(lx)\}_{l \in \mathbb{N}_0}$  is a basis and  $L$  is linear the condition that  $\phi \in \text{Ker } L$  means that there is at least one integer  $k \in \mathbb{N}_0$  such that  $L(\alpha \cos(kx)) = (dk^2 - i + \zeta_0 - Dg(a_0))\alpha \cos(kx) = 0$  for some  $\alpha = (\text{Re } \alpha, \text{Im } \alpha) \in \mathbb{C} \setminus \{0\}$ . Using Eq. (A4) it follows that  $dk^2$  must be an eigenvalue of the matrix

$$N = \begin{pmatrix} -\zeta_0 + 3(\text{Re } a_0)^2 + (\text{Im } a_0)^2 & 2 \text{Re } a_0 \text{Im } a_0 - 1 \\ 2 \text{Re } a_0 \text{Im } a_0 + 1 & -\zeta_0 + (\text{Re } a_0)^2 + 3(\text{Im } a_0)^2 \end{pmatrix} \quad (\text{A6})$$

with eigenvector  $\alpha$ . Non-zero elements in  $\text{Ker } L$  exist if  $\det(-dk^2 \text{Id} + N) = 0$  and computing this determinant yields

$$(\zeta_0 + dk^2)^2 - 4|a_0(\zeta_0)|^2(\zeta_0 + dk^2) + 1 + 3|a_0(\zeta_0)|^4 = 0. \quad (\text{A7})$$

Solving for  $k$  leads to  $k_{1,2}$  given by the following equation:

$$k_{1,2} := \sqrt{\frac{2|a_0(\zeta_0)|^2 - \zeta_0 \pm \sqrt{|a_0(\zeta_0)|^4 - 1}}{d}}. \quad (\text{A8})$$

Likewise, non-zero elements in  $\text{Ker } L^*$  exist if  $\det(-d\tilde{k}^2 \text{Id} + N^T) = 0$  for some integer  $\tilde{k} \in \mathbb{N}_0$ . Since  $\det(-d\tilde{k}^2 \text{Id} + N^T) = \det(-d\tilde{k}^2 \text{Id} + N)$ , this leads to the same formula (A8) for  $\tilde{k}_{1,2}$ . In the remaining part of this section we write  $k$  as a shorthand for one of the two values  $k_{1,2}$ . Consequently, under the condition (A7) there is a vector  $\alpha$  and a vector  $\alpha^*$  such that  $\alpha \cos(kx) \in \text{Ker } L$  and  $\alpha^* \cos(kx) \in \text{Ker } L^*$ .

Now we determine  $\alpha$  and  $\alpha^*$  under the condition (A7). In the matrix  $N - dk^2 \text{Id}$  the first or the second line could be zero (but not both). Therefore, the eigenvector  $\alpha$  of (A6) is given in the form

$$\alpha = \begin{pmatrix} 2 \text{Re } a_0 \text{Im } a_0 - 1 \\ \zeta + dk^2 - 3(\text{Re } a_0)^2 - (\text{Im } a_0)^2 \end{pmatrix} \text{ or } \alpha = \begin{pmatrix} \zeta + dk^2 - (\text{Re } a_0)^2 - 3(\text{Im } a_0)^2 \\ 2 \text{Re } a_0 \text{Im } a_0 + 1 \end{pmatrix} \quad (\text{A9})$$

such that  $(-dk^2 \text{Id} + N)\alpha = 0$ , and hence  $\alpha \cos(kx)$  belongs to  $\text{Ker } L$ . The first choice can be taken if  $2 \text{Re } a_0 \text{Im } a_0 - 1 \neq 0$  and the second choice if  $2 \text{Re } a_0 \text{Im } a_0 + 1 \neq 0$ . Likewise,

$$\alpha^* = \begin{pmatrix} \zeta + dk^2 - (\text{Re } a_0)^2 - 3(\text{Im } a_0)^2 \\ 2 \text{Re } a_0 \text{Im } a_0 - 1 \end{pmatrix} \text{ or } \alpha^* = \begin{pmatrix} 2 \text{Re } a_0 \text{Im } a_0 + 1 \\ \zeta + dk^2 - 3(\text{Re } a_0)^2 - (\text{Im } a_0)^2 \end{pmatrix} \quad (\text{A10})$$

with  $\alpha^* = (\text{Re } \alpha^*, \text{Im } \alpha^*) \in \mathbb{C}$  satisfies  $(-dk^2 \text{Id} + N^T)\alpha^* = 0$  and leads to an element  $\alpha^* \cos(kx) \in \text{Ker } L^*$ . As before, the first choice can be taken if  $2 \text{Re } a_0 \text{Im } a_0 - 1 \neq 0$  and the second choice if  $2 \text{Re } a_0 \text{Im } a_0 + 1 \neq 0$ .

We can exclude the case  $k_1 = 0$  or  $k_2 = 0$  in the bifurcation condition (A7) since it would only lead to bifurcation of trivial solutions, and we are interested in non-trivial solutions. The kernel of  $L$  will be one-dimensional provided that in Eq. (A7) we have  $k_1 \in \mathbb{N}$  and  $k_2 \notin \mathbb{N}$  or vice versa, and two-dimensional if both  $k_1, k_2 \in \mathbb{N}$ . If neither  $k_1$  or  $k_2$  are in  $\mathbb{N}$ , then  $\text{Ker } L = \text{Ker } L^* = \{0\}$ , and the implicit function theorem (cf. [26, Theorem I.1.1]) implies that solutions nearby the point  $(\zeta_0, a_0)$  are unique, and therefore trivial. Hence,  $(\zeta_0, a_0)$  cannot be a bifurcation point in this case, and therefore the necessary bifurcation condition is that  $k_1 \in \mathbb{N}$  or  $k_2 \in \mathbb{N}$ . The same condition, expressed in the form of Eq. (A7), is given in [21, Proposition 10].

## APPENDIX B: TRANSVERSALITY CONDITION

According to the Crandall-Rabinowitz theorem (cf. [37, Theorem I.5.1] and [26]) two conditions are sufficient for bifurcation. The first is that  $\text{Ker } L$  is one-dimensional, i.e., with  $k_1, k_2$  from (A8), we need that  $k_1 \in \mathbb{N}$ ,  $k_2 \notin \mathbb{N}$  or vice versa, and we write  $k$  for the one which is the integer. As we will see the second condition (the transversality condition) is given by

$$2|a_0(\zeta_0)|^4(|a_0(\zeta_0)|^2 - \zeta_0) \mp (1 + \zeta_0^2 - |a_0(\zeta_0)|^4)\sqrt{|a_0(\zeta_0)|^4 - 1} \neq 0 \quad (\text{B1})$$

with “ $-$ ” if  $k_1 \in \mathbb{N}$  and “ $+$ ” if  $k_2 \in \mathbb{N}$ . To verify that (B1) together with the one-dimensionality of the kernel is really sufficient for bifurcation we need to bring our problem into the form used in [37]. Nontrivial solutions of Eqs. (A1), (A2) may be written as  $a(x) = a_0(\zeta) + b(x)$  with  $b'(0) = b'(\pi) = 0$ . From Eqs. (A1), (A2) we derive the equation for the function  $b$  in the form

$$F(\zeta, b) := -db'' - (i - \zeta)(a_0(\zeta) + b) - g(a_0(\zeta) + b) = 0 \quad (\text{B2})$$

where  $F$  is defined on  $\mathbb{R} \times H$  with  $H$  given as the real Hilbert space of twice almost everywhere differentiable functions  $b : [0, \pi] \rightarrow \mathbb{C}$  with  $b'(0) = b'(\pi) = 0$  and  $b, b''$  being square integrable. Notice that  $F(\zeta, 0) = 0$  for all  $\zeta$ , i.e., the curve of trivial solutions  $(\zeta, a_0(\zeta))$  for Eqs. (A1), (A2) has now become the line of zero solutions  $(\zeta, 0)$  for Eq. (B2). Let us write  $D_{b, \zeta}^2 F(\zeta_0, 0)$  for the mixed second derivative of  $F$  with respect to  $b$  and  $\zeta$  at the point  $(\zeta_0, 0)$ . In our case, where  $F$  is defined by (B2) we find for the mixed second derivative

$$D_{b, \zeta}^2 F(\zeta_0, 0)\phi = \phi - D^2 g(a_0)(\phi, \dot{a}_0) = \phi - 2\bar{a}_0 \phi \dot{a}_0 - 2a_0 \bar{\phi} \dot{\bar{a}}_0 - 2a_0 \bar{\phi} \dot{a}_0 \quad (\text{B3})$$

where  $\dot{a}_0 = \frac{d}{d\zeta}a_0(\zeta)|_{\zeta=\zeta_0}$  is the tangent direction along the curve  $\zeta \mapsto a_0(\zeta)$  at the point  $\zeta_0$ . According to [37], the transversality condition is expressed by

$$D_{b,\zeta}^2 F(\zeta_0, 0)\phi \notin \text{Rg}(D_b F(\zeta_0, 0)),$$

with  $\phi$  such that  $\text{Ker}(D_b F(\zeta_0, 0)) = \text{span}\{\phi\}$ . In our case  $D_b F(\zeta_0, 0) = L$ , where  $L$  is the linearized operator given in Eq. (A3). By the Fredholm alternative, cf. [38],  $\text{Rg} L = (\text{Ker} L^*)^\perp = \text{span}\{\phi^*\}^\perp$ , where  $\phi(x) = \alpha \cos(kx)$ ,  $\phi^*(x) = \alpha^* \cos(kx)$  with  $\alpha$  from Eq. (A9) and  $\alpha^*$  from Eq. (A10). Here orthogonality  $u \perp v$  of two functions  $u, v \in H$  is understood as vanishing of the inner product  $\langle u, v \rangle = \text{Re} \int_0^\pi u(x)\bar{v}(x) dx$ . Hence, transversality is expressed as

$$\langle D_{b,\zeta}^2 F(\zeta_0, 0)\phi, \phi^* \rangle = \text{Re} \int_0^\pi (D_{b,\zeta}^2 F(\zeta_0, 0)\phi)\bar{\phi}^* dx \neq 0 \quad (\text{B4})$$

and we will show next that this amounts to

$$\langle D_{b,\zeta}^2 F(\zeta_0, 0)\phi, \phi^* \rangle = \frac{-\pi(2 \text{Re} a_0 \text{Im} a_0 \mp 1)}{3|a_0|^4 - 4|a_0|^2\zeta_0 + \zeta_0^2 + 1} \left( (dk^2 - \zeta_0)|a_0|^4 + (\zeta_0^2 + 1)(2|a_0|^2 - dk^2 - \zeta_0) \right). \quad (\text{B5})$$

In order to evaluate  $D_{b,\zeta}^2 F(\zeta_0, 0)\phi$  we first need to determine the tangent  $\dot{a}_0 = \frac{d}{d\zeta}a_0(\zeta)|_{\zeta=\zeta_0}$ . Differentiating the equation  $(i - \zeta)a_0(\zeta) + g(a_0(\zeta)) = 0$  with respect to  $\zeta$  and evaluating the derivative at  $\zeta_0$  we get

$$(Dg(a_0) + i - \zeta_0)\dot{a}_0 = a_0.$$

Recalling that  $Dg(a_0)z = 2|a_0|^2z + a_0^2\bar{z}$  we thus find

$$(2|a_0|^2 + i - \zeta_0)\dot{a}_0 + a_0^2\bar{\dot{a}_0} = a_0$$

and hence

$$\dot{a}_0 = \tau a_0 \quad \text{with} \quad \tau = \frac{|a_0|^2 - \zeta_0 - i}{3|a_0|^4 - 4|a_0|^2\zeta_0 + \zeta_0^2 + 1}. \quad (\text{B6})$$

Inserting  $\dot{a}_0$  from Eq. (B6) into Eq. (B3) we deduce that the transversality condition (B4) becomes

$$\langle D_{b,\zeta}^2 F(\zeta_0, 0)\phi, \phi^* \rangle = \frac{\pi}{2} \text{Re} \left( \alpha\bar{\alpha}^* - 4 \text{Re} \tau |a_0|^2 \alpha\bar{\alpha}^* - 2\tau a_0^2 \bar{\alpha}\bar{\alpha}^* \right) \neq 0 \quad (\text{B7})$$

Depending on the alternatives in Eqs. (A9), (A10) for the actual form of  $\alpha, \alpha^*$  we obtain

$$\text{Re} \alpha\bar{\alpha}^* = (2 \text{Re} a_0 \text{Im} a_0 \mp 1)(2\zeta_0 + 2dk^2 - 4|a_0|^2).$$

Likewise

$$\begin{aligned} \bar{\alpha}\bar{\alpha}^* &= (2 \text{Re} a_0 \text{Im} a_0 \mp 1)(\zeta_0 + dk^2 - (\text{Re} a_0)^2 - 3(\text{Im} a_0)^2) - (2 \text{Re} a_0 \text{Im} a_0 \mp 1)(\zeta_0 + dk^2 - 3(\text{Re} a_0)^2 - \text{Im}(a_0)^2) \\ &\quad - i \left( (2 \text{Re} a_0 \text{Im} a_0 \mp 1)^2 + \underbrace{(\zeta_0 + dk^2 - 3(\text{Re} a_0)^2 - (\text{Im} a_0)^2)(\zeta_0 + dk^2 - (\text{Re} a_0)^2 - 3(\text{Im} a_0)^2)}_{\stackrel{(\text{A7})}{=} 4(\text{Re} a_0)^2 \text{Im}(a_0)^2 - 1} \right) \\ &= (2 \text{Re} a_0 \text{Im} a_0 \mp 1) 2\bar{a}_0^2 \end{aligned}$$

where we have used the necessary bifurcation condition (A7). Taking the expressions for  $\text{Re} \alpha\bar{\alpha}^*$  and  $a_0^2 \bar{\alpha}\bar{\alpha}^*$  into the transversality condition (B7) finally leads to

$$\begin{aligned} \langle D_{b,\zeta}^2 F(\zeta_0, 0)\phi, \phi^* \rangle &= \frac{\pi}{2} \text{Re} \left( \alpha\bar{\alpha}^* - 4 \text{Re} \tau |a_0|^2 \alpha\bar{\alpha}^* - 2\tau a_0^2 \bar{\alpha}\bar{\alpha}^* \right) \\ &= \frac{\pi}{2} (2 \text{Re} a_0 \text{Im} a_0 \mp 1) \left( (2\zeta_0 + 2dk^2 - 4|a_0|^2)(1 - 4 \text{Re} \tau |a_0|^2) - 4 \text{Re} \tau |a_0|^4 \right) \neq 0. \end{aligned}$$

Since the choice in Eqs. (A9), (A10) was made so that the factor  $(2 \text{Re} a_0 \text{Im} a_0 \mp 1)$  is non-zero, the non-vanishing of the expression in brackets amounts to (after inserting  $\text{Re} \tau = \frac{|a_0|^2 - \zeta_0}{3|a_0|^4 - 4|a_0|^2\zeta_0 + \zeta_0^2 + 1}$ )

$$(dk^2 - \zeta_0)|a_0|^4 + (\zeta_0^2 + 1)(2|a_0|^2 - dk^2 - \zeta_0) \neq 0.$$

We have therefore verified (B5), and using the definition  $k_1, k_2$  from Eq. (A8) we obtain the transversality condition in its final form (B1), where only  $a_0$  and  $\zeta_0$  appear.

**APPENDIX C: APPROXIMATIONS FOR THE BRIGHT-SOLITON POWER CONVERSION EFFICIENCY  $\eta_{\text{BS,max}}$  AND COMB BANDWIDTH  $2k_{\text{BS,max}}^*$**

For bright solitons, a closed form approximation [12, 31–34] of the intracavity field is given by

$$a(x) \approx \Psi_0 + \Psi_1(x) = \Psi_0 + B e^{i\varphi_0} \operatorname{sech} \left( \frac{B}{\sqrt{2d}} x \right). \quad (\text{C1})$$

Here,  $\Psi_1(x)$  represents the field of a bright soliton on top of a constant background field  $\Psi_0$ ,  $B \approx \sqrt{2\zeta}$  defines the width and the amplitude of the soliton, and  $\varphi_0 = \arccos \left( \frac{\sqrt{8\zeta}}{\pi f} \right)$  is the relative phase of the soliton with respect to  $\Psi_0$ . For strong solitons, the intracavity field will be dominated by the soliton itself, such that  $a(x) \approx \Psi_1(x)$ . For a given forcing, the maximum detuning can be derived by the condition that the argument of the arccos function may not exceed 1, cf. supplementary information in [12]. For a maximum detuning  $\zeta_{\text{max}} = \frac{\pi^2 f^2}{8}$ ,  $\varphi = 0$  and the intracavity field reads

$$a(x) \approx \frac{\pi f}{2} \operatorname{sech} \left( \frac{\pi f}{2\sqrt{2d}} x \right). \quad (\text{C2})$$

Given this expression, the power conversion efficiency at the maximum detuning for bright solitons can be computed by an integral in the spatial domain,

$$\eta_{\text{BS,max}} = \frac{\frac{1}{2\pi} \int_{-\pi}^{\pi} \left| \frac{\pi f}{2} \operatorname{sech} \left( \frac{\pi f}{2\sqrt{2d}} x \right) \right|^2 dx}{f^2} = \frac{1}{f} \sqrt{\frac{d}{2}} \tanh \left( \frac{\pi f}{2\sqrt{2d}} \pi \right) \approx \frac{1}{f} \sqrt{\frac{d}{2}}. \quad (\text{C3})$$

In order to determine the comb bandwidth, we calculate the Fourier coefficients associated with the various comb lines. The power spectrum is given by the magnitude square of these coefficients,

$$\begin{aligned} |\hat{a}_k|^2 &= \left| \frac{1}{2\pi} \int_{-\pi}^{\pi} \frac{\pi f}{2} \operatorname{sech} \left( \frac{\pi f}{2\sqrt{2d}} x \right) e^{-ikx} dx \right|^2 \\ &\approx \left| \frac{1}{2\pi} \int_{-\infty}^{\infty} \frac{\pi f}{2} \operatorname{sech} \left( \frac{\pi f}{2\sqrt{2d}} x \right) e^{-ikx} dx \right|^2 = \frac{d}{2} \operatorname{sech}^2 \left( \frac{\sqrt{2d}}{f} k \right). \end{aligned} \quad (\text{C4})$$

The full-width at half-maximum bandwidth  $x_{\text{FWHM}}$  of the  $\operatorname{sech}^2$  function is given by the condition

$$\operatorname{sech}^2 \left( \frac{x_{\text{FWHM}}}{2} \right) = \frac{1}{2}, \quad (\text{C5})$$

which leads to  $x_{\text{FWHM}} = 2 \ln(1 + \sqrt{2})$ . This leads to the FWHM bandwidth  $2k_{\text{BS,max}}^*$ ,

$$2k_{\text{BS,max}}^* = \frac{f}{\sqrt{2d}} x_{\text{FWHM}} = \sqrt{2} \ln(1 + \sqrt{2}) \frac{f}{\sqrt{d}}. \quad (\text{C6})$$

For a representation of the Eqs. (C3) and (C6) in physical, i.e., non-normalized units, see, e.g., [31, 32].

**APPENDIX D: PHYSICAL POWER CONVERSION EFFICIENCY OUTSIDE OF THE MICRORESONATOR**

In physical terms, the time-dependent Lugiato-Lefever equation [39] is given by

$$T_R \frac{\partial E(T, \tau)}{\partial T} = \sqrt{\kappa} \sqrt{P_{\text{in}}} + \left( -\frac{\alpha}{2} - \frac{\kappa}{2} - i\delta_0 - i\frac{\beta_2}{2} L \frac{\partial^2}{\partial \tau^2} + i\gamma L |E(T, \tau)|^2 \right) E(T, \tau). \quad (\text{D1})$$

Here,  $T_R$  is the round-trip time of light circulating in the resonator,  $E$  the electric field,  $T$  the physical time,  $\tau$  the round-trip position inside the resonator,  $\kappa$  the power-coupling coefficient of the bus waveguide and the microresonator,  $P_{\text{in}}$  the power of the pump light,  $\alpha$  the power round-trip loss,  $\beta_2$  the second order dispersion coefficient,  $L$  the circumference, and  $\gamma$  the nonlinearity coefficient of the microresonator. The detuning  $\delta_0 = (\omega_r - \omega_p) T_R$  is defined

by the difference between the angular frequency of the pump laser  $\omega_p$ , the angular resonance frequency  $\omega_r$  and the round-trip time.

The normalized field  $a(t, x)$  for  $x \in [0, 2\pi)$  and the normalized quantities  $\zeta$  and  $d$  satisfy the time-dependent normalized Lugiato-Lefever equation

$$\frac{\partial a(t, x)}{\partial t} = f + \left( -1 - i\zeta + id \frac{\partial^2}{\partial x^2} + i|a(t, x)|^2 \right) a(t, x),$$

and are related to the physical parameters  $E$  and  $P_{\text{in}}$ ,  $\gamma$ ,  $\alpha$ ,  $\kappa$ ,  $\delta_0$ ,  $T_R$  and  $\beta_2$  via

$$a(t, x) = \sqrt{\frac{2\gamma L}{\alpha + \kappa}} E(T, \tau), \quad (\text{D2})$$

$$t = \frac{\alpha + \kappa}{2} \frac{T}{T_R}, \quad (\text{D3})$$

$$x = \frac{2\pi}{T_R} \tau, \quad (\text{D4})$$

$$f = \sqrt{\frac{2\gamma L}{\alpha + \kappa}} \frac{2\sqrt{\kappa}}{\alpha + \kappa} \sqrt{P_{\text{in}}}, \quad (\text{D5})$$

$$\zeta = \frac{2\delta_0}{\alpha + \kappa}, \quad (\text{D6})$$

$$d = \frac{-4\pi^2 \beta_2 L}{(\alpha + \kappa) T_R^2}. \quad (\text{D7})$$

For the field  $E(T, \tau) = \sum_{k \in \mathbb{Z}} \hat{E}_k(T) e^{ik2\pi\tau/T_R}$ , the intracavity-power is given by  $\frac{1}{T_R} \int_0^{T_R} |E(T, \tau)|^2 d\tau = \sum_{k \in \mathbb{Z}} |\hat{E}_k|^2$ . The power of the frequency comb is defined as power of the intracavity-field excluding the pumped mode,  $P_{\text{p,FC}} = \sum_{k \in \mathbb{Z} \setminus \{0\}} |\hat{E}_k|^2$ . The pumped mode is excluded since it will have a non-zero value even if no frequency comb is formed. The physical power conversion efficiency  $\eta_{\text{in}}$  inside the microresonator can then be expressed as

$$\eta_{\text{in}} = \frac{P_{\text{p,FC}}}{P_{\text{in}}} = \frac{\sum_{k \in \mathbb{Z} \setminus \{0\}} |\hat{E}_k|^2}{P_{\text{in}}}. \quad (\text{D8})$$

When the comb is coupled out of the microresonator, the field amplitude is decreased by the square root of the power-coupling coefficient  $\kappa$ . Therefore, the physical conversion efficiency with respect to the comb power outside of the resonator  $\eta_{\text{out}}$  is given by

$$\eta_{\text{out}} := \frac{\sum_{k \in \mathbb{Z} \setminus \{0\}} |\sqrt{\kappa} \hat{E}_k|^2}{P_{\text{in}}} = \kappa \eta_{\text{in}}. \quad (\text{D9})$$

Given the relations (D2), (D5), the normalized power conversion efficiency  $\eta$  defined as the ratio between the power of the normalized frequency comb  $\sum_{k \in \mathbb{Z} \setminus \{0\}} |\hat{a}_k|^2$  and the normalized forcing power  $f^2$  can be expressed by physical quantities as follows

$$\eta = \frac{\sum_{k \in \mathbb{Z} \setminus \{0\}} |\hat{a}_k|^2}{f^2} = \frac{\sum_{k \in \mathbb{Z} \setminus \{0\}} \left| \sqrt{\frac{2\gamma L}{\alpha + \kappa}} \hat{E}_k \right|^2}{\left( \sqrt{\frac{2\gamma L}{\alpha + \kappa}} \frac{2\sqrt{\kappa}}{\alpha + \kappa} \sqrt{P_{\text{in}}} \right)^2} = \frac{(\alpha + \kappa)^2}{4\kappa} \eta_{\text{in}} = \frac{(\alpha + \kappa)^2}{4\kappa^2} \eta_{\text{out}}. \quad (\text{D10})$$

This is equivalent to Eq. (11) of the main manuscript.

- 
- [1] J. Pfeifle, A. Coillet, R. Henriët, K. Saleh, P. Schindler, C. Weimann, W. Freude, I. V. Balakireva, L. Larger, C. Koos, and Y. K. Chembo, Phys. Rev. Lett. **114**, 1 (2015).  
 [2] J. Pfeifle, V. Brasch, M. Lauer mann, Y. Yu, D. Wegner, T. Herr, K. Hartinger, P. Schindler, J. Li, D. Hillerkuss, R. Schmogrow, C. Weimann, R. Holzwarth, W. Freude, J. Leuthold, T. J. Kippenberg, and C. Koos, Nat. Photon. **8**, 375 (2014).

- [3] P. Marin-Palomo, J. N. Kemal, M. Karpov, A. Kordts, J. Pfeifle, M. H. Pfeiffer, P. Trocha, S. Wolf, V. Brasch, M. H. Anderson, R. Rosenberger, K. Vijayan, W. Freude, T. J. Kippenberg, and C. Koos, *Nature* **546**, 274 (2017).
- [4] M.-G. Suh and K. Vahala, *Science* **887**, 884 (2017).
- [5] P. Trocha, M. Karpov, D. Ganin, M. H. Pfeiffer, A. Kordts, S. Wolf, J. Krockenberger, P. Marin-Palomo, C. Weimann, S. Randel, W. Freude, T. J. Kippenberg, and C. Koos, *Science* **359**, 887 (2018).
- [6] M.-G. Suh, Q.-F. Yang, K. Y. Yang, X. Yi, and K. Vahala, *Science* **6516**, 600 (2016).
- [7] D. T. Spencer, T. Drake, T. C. Briles, J. Stone, L. C. Sinclair, C. Fredrick, Q. Li, D. Westly, B. R. Ilic, A. Bluestone, N. Volet, T. Komljenovic, L. Chang, S. H. Lee, D. Y. Oh, M. G. Suh, K. Y. Yang, M. H. Pfeiffer, T. J. Kippenberg, E. Norberg, L. Theogarajan, K. Vahala, N. R. Newbury, K. Srinivasan, J. E. Bowers, S. A. Diddams, and S. B. Papp, *Nature* **557**, 81 (2018).
- [8] M. H. P. Pfeiffer, C. Herkommer, J. Liu, H. Guo, M. Karpov, E. Lucas, M. Zervas, and T. J. Kippenberg, *Optica* **4**, 684 (2017).
- [9] C. Joshi, J. K. Jang, K. Luke, X. Ji, S. A. Miller, A. Klenner, Y. Okawachi, M. Lipson, and A. L. Gaeta, *Opt. Lett.* **41**, 2565 (2016).
- [10] J. Liu, A. S. Raja, M. Karpov, B. Ghadiani, M. H. P. Pfeiffer, B. Du, N. J. Engelsen, H. Guo, M. Zervas, and T. J. Kippenberg, *Optica* **5**, 3 (2018).
- [11] T. J. Kippenberg, R. Holzwarth, and S. A. Diddams, *Science* **332**, 555 (2011).
- [12] T. Herr, V. Brasch, J. D. Jost, C. Y. Wang, N. M. Kondratiev, M. L. Gorodetsky, and T. J. Kippenberg, *Nat. Photon.* **8**, 145 (2014).
- [13] L. Lugiato and R. Lefever, *Phys. Rev. Lett.* **58**, 2209 (1987).
- [14] C. Godey, I. V. Balakireva, A. Coillet, and Y. K. Chembo, *Phys. Rev. A* **89**, 063814 (2014).
- [15] P. Parra-Rivas, D. Gomila, L. Gelens, and E. Knobloch, *Phys. Rev. E* **97**, 042204 (2018).
- [16] H. Guo, M. Karpov, E. Lucas, A. Kordts, V. Pfeiffer, Martin H. P. Brasch, G. Lichachev, V. E. Lobanov, M. L. Gorodetsky, and T. J. Kippenberg, *Nat. Phys.* **13**, 94 (2016).
- [17] X. Yi, Q.-F. Yang, K. Y. Yang, M.-G. Suh, and K. Vahala, *Optica* **2**, 1078 (2015).
- [18] C. Godey, *Eur. Phys. J. D* **71**, 131 (2017).
- [19] P. Parra-Rivas, D. Gomila, M. A. Matias, S. Coen, and L. Gelens, *Phys. Rev. A* **89**, 043813 (2014).
- [20] P. Parra-Rivas, E. Knobloch, D. Gomila, and L. Gelens, *Phys. Rev. A* **93**, 1 (2016).
- [21] R. Mandel and W. Reichel, *SIAM J. Appl. Math.* **77**, 315 (2017).
- [22] T. Miyaaji, I. Ohnishi, and Y. Tsutsumi, *Physica D* **239**, 2066 (2010).
- [23] L. Delcey and M. Haragus, *Philos. Trans. of the Roy. Soc. A* **376**, 20170188 (2018).
- [24] M. Stanislavova and A. G. Stefanov, *J. Math. Phys.* **59**, 101502, 12 (2018).
- [25] X. Xue, Y. Xuan, Y. Liu, P.-H. Wang, S. Chen, J. Wang, D. E. Leaird, M. Qi, and A. M. Weiner, *Nat. Photon.* **9**, 594 (2015).
- [26] H. Kielhöfer, *Bifurcation theory*, Applied Mathematical Sciences, Vol. 156 (Springer, New York, 2012).
- [27] P. H. Rabinowitz, *J. Functional Analysis* **7**, 487 (1971).
- [28] R. Mandel, “Global secondary bifurcation, symmetry breaking and period-doubling,” (2018), arXiv:1803.04903v1.
- [29] H. Uecker, D. Wetzler, and J. D. Rademacher, *NMTMA* **7**, 58 (2014).
- [30] T. Dohnal, J. Rademacher, H. Uecker, and D. Wetzler, in *European Nonlinear Dynamics Conference (ENOC)* (2014) p. 373.
- [31] S. Coen and M. Erkintalo, *Opt. Lett.* **38**, 1790 (2013).
- [32] C. Bao, L. Zhang, A. Matsko, Y. Yan, Z. Zhao, G. Xie, A. M. Agrawal, L. C. Kimerling, J. Michel, L. Maleki, and A. E. Willner, *Opt. Lett.* **39**, 6126 (2014).
- [33] K. Nozaki and N. Bekki, *J. Phys. Soc. Jpn* **54**, 2363 (1985).
- [34] K. Nozaki and N. Bekki, *Physica D* **21**, 381 (1986).
- [35] X. Xue, P. H. Wang, Y. Xuan, M. Qi, and A. M. Weiner, *Laser Photonics Rev.* **11**, 1 (2017).
- [36] J. Gärtner, R. Mandel, and W. Reichel, “The Lugiato-Lefever equation with nonlinear damping caused by two photon absorption,” (2018), arXiv:1811.12200.
- [37] M. G. Crandall and P. H. Rabinowitz, *J. Functional Analysis* **8**, 321 (1971).
- [38] H. Brezis, *Functional analysis, Sobolev spaces and partial differential equations*, Universitext (Springer, New York, 2011).
- [39] T. Hansson and S. Wabnitz, *Nanophotonics* **5**, 231 (2016).